New Method for [18]FDG generating using Geant4/Gate7

Abuzar Shakeri[1], Ebrahim Heidari[2], Nasrin Hoseini Motlagh[3*], Hamid Reza Vanaei[2]

1. Department of Nuclear Engineering, Bushehr Branch, Islamic Azad University, Bushehr, Iran
2. Department of Sciences, Bushehr Branch, Islamic Azad University, Bushehr, Iran
3. Department of Physics, Shiraz Branch, Islamic Azad University, Shiraz, Iran

Email:nasrinhosseinimotlagh@gmail.com, hosseinimotlagh@iaushiraz.ac.ir

ABSTRACT

Fluorine 18-deoxyglucose is often used in Positron Emission Tomography devices. Positron Emission Tomography imaging is one of the useful tool which is used for cancer detection and its management. Positron Emission Tomography growth is limited due to problems that depend on the production of Fluorine-18. Imaging results are strongly depending on the information of nuclear reaction cross section data. This study is presented to calculate different quantities such as stopping power, CSDA range, simulated and distributed absorbed dose of Fluorine-18 in water. In order to access these goals, we use Geant4/Gate7 simulation and the Bethe-Bloch model. The results of this simulation and theoretical model presented are in good agreement with each other. The important point of this paper is the presentation of a theoretical approach in order to the production of Fluorine-18 using protons generated through the main $D(d;p)T$ and side $^3He(d;p)^4He$ nuclear fusion reaction in which uses Helium-3 is catalyzed.

Keywords: Fluorine-18, Fusion, Stopping power, Absorbed dose, Proton

INTRODUCTION:

Positron emission tomography (PET) has established itself as a very special and sensitive tool for early detection, staging and follow-up of cancer, imaging molecular interactions and pathways inside the human body [1-4]. In general, imaging is possible in two ways: i. Anatomical (in MRI, CT), ii. Functional (in SPECT, PET). In the case of anatomy, only anatomy of the organs is visible, and therefore a lesion is detectable when its physical characteristics have changed (for example, the X-ray absorption coefficient in CT imaging or its proton density has changed in MRI imaging). If the physical characteristics of an organ have changed so much that it is visible in CT imaging, practically it will be impossible to implement early and timely treatments. But in the functional imaging technique, the metabolic function of the tissue is visible before changing its physical characteristics. The metabolic changes have begun long before physical changes, and therefore functional imaging can provide early treatment before disease progresses. Although MRI and CT functional are also available today, the sensitivity of these methods is still far below the ideal standards in nuclear medicine. PET imaging is based on the injection and distribution of the radio drug positron emission into the patient's body.

The purpose of the imaging via injection of radioactive matter is detection of the radio drug site accumulation in the tissue. But in the PET technique instead of the positron accumulation site, its destruction site is visible. If the positron range is longer, then the error will be greater. Therefore, the substances selected as radioactive drugs for injecting to patient's body should contain positrons with a low kinetic energy, so that, they cannot traverse large distances in the tissue (such as ^{18}F). As already mentioned, PET is potentially a very useful the distribution of a tool for monitoring deposited dose at the patient's body using proton therapy [1-8]. This method is based on the detection of the positron annihilation of γ rays following the decay of small amounts of positron emitters (typically ^{11}C , ^{13}N and ^{15}O) generated by non-elastic nuclear reaction of protons with target nuclei under radiation. Approval of treatment can be achieved comparing the PET images with detecting the distribution of positron activity with the predicted dose distribution used for treatment.

PET imaging basically reflects the distribution of energy deposited, since the cross sections of the inelastic nuclear reactions signal are along the path of the beam, but at the Bragg peak, the greatest deposited energy of the proton through other interactions be reduced. However, comparing the distribution of the measured radioisotope with PET, it is possible to confirm the effective dose with efficiency of the predicted positron emitters from the program code therapy. The possibility of monitoring on the proton therapy using PET by various groups has been investigated [2, 8].

A number of MC simulation tools are made for imaging or dosimetry [11]. Currently, Gate (Geant-4 Application for Emission Tomography) is the only open source MC simulation platform that supports user-friendly imaging simulation, RT and dosimetry simulations in the same region. Gate is a Geant-4 toolkit-based application. Geant-4 manages a kernel that simulates particle-material interactions, and Gate creates extra high-level features to facilitate the design of Geant-4-based simulations. Gate is generally useful for a wide range of simulations, for example in determining absorbed dose in cancerous tissue. While Gate has been widely endorsed and used for a wide range of PET and SPECT studies, there are still a limited number of articles reporting its application and reliability in the dosimetry branch [12].

Due to electronic interactions, charged particles as they pass through a medium, losing energy in the process and slowing down. As the particle slows down, ionizations density induced in the medium increases, before. Ionization density drops suddenly to zero beyond the Bragg peak, because all the kinetic energy of the particle reaches zero it can be considered stationary. Under certain conditions, the relativistic Bethe Eq. is used for determining the stopping power in a medium [13]. Ziegler, showed that further corrections such as Barkas, Bloch and Fermi can be made to account for high energy particles and high atomic number targets [14]. The average of
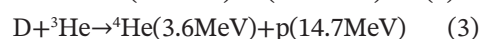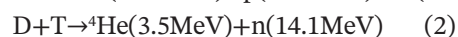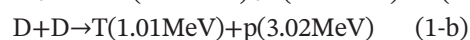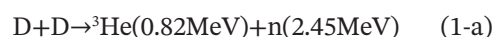
charged particles path length in an unbounded uniform medium is defined as the range at a given energy. It can be calculated theoretically by the integral of the reciprocal of the stopping power over energy from zero to the initial value. This integral is known as the continuous slowing-down approximation (CSDA) range.

Nowadays, ^{18}F can be produced using particle accelerators, especially cyclotrons, but the purpose of this research is utilization of generated protons from the DD fusion reaction through the fast ignition in inertial confinement fusion as a new source of protons to produce ^{18}F via the ^{18}O(p.n)^{18}F nuclear reaction in order to PET imaging. It should be noted that the energy released from this fusion reaction is a clean energy and it can be convert to electric energy .Therefore, in this paper, at first we calculate the proton flux required for the production of ^{18}F using fast ignition of the D-D fusion reaction via a ^{3}He catalyzed. Then, the cross-section and the rate production of ^{18}F, saturation coefficient, yield production of ^{18}F, and followed by stopping power, CSDA range, absorbed dose of ^{18}F in water using the Gate and compare it with the Bethe-Bloch model and we will examine the consistency of it. Also we represent the steps in the synthesis and purification of FDG, specially irradiation of ^{18}O water with protons, in order to the cost reduction of FDG production.

2-Calculation of the proton flux produced by fast ignition of D-D fusion reaction via the ^{3}He catalyzed in ^{18}F production

In 1994, Tabak et.al, proposed a fast ignition method as a suitable alternative to inertial fusion methods. In this method, unlike the central hot spot ignition method, the compression and ignition processes are separated separately to reduce the hydrodynamic instabilities and to achieve higher energy efficiency. In this method, the fuel capsule is compressed firstly at a low temperature by laser or ion beams to high areal density $\rho R=2\text{-}3gcm^{-2}$. Then at time interval 10-50ps ,a laser beam is used with a power higher than 10^{18} W and a very short wavelength of 0.2 in order to ignition [9-11].A number of fusion researchers are developing on the deuterium and tritium (D-T) fusion energy sources due to relatively large

reaction rate. Although the great D-T fusion reactivity has attracted fusion researchers, however, D-T burning has its own serious problems because tritium inventory in nature is very low and must be artificially produced (using the reaction (n (6Li, T)). Providing adequate ratios of further tritium generation will pose a serious challenge to power plant design. In addition, tritium is a radioactive substance. As well as the control of 14.1MeV neutrons from D-T fusion reaction, are difficult. While D-^{3}He fusion reaction does not produce much energetic neutrons. Also, like tritium, ^{3}He is not abundant on the surface of the earth. Therefore, D-D fusion reaction may be the most interesting because eliminates the problem of high-energy neutrons related to the D-T reaction, although it has a relatively small fusion reaction cross section [12, 13]. The direct consequence of this reaction is that it reduces the amount of waste in fusion plasma that impedes ignition in laser fusion. The D-D cycle only uses deuterium as a fuel, which can even be extracted from seawater [9-11]. In a fusion reactor with D-D fuel, the fusion reactions occur from the following four channels:

$$D+D\rightarrow {}^3He(0.82MeV)+n(2.45MeV) \quad \text{(1-a)}$$
$$D+D\rightarrow T(1.01MeV)+p(3.02MeV) \quad \text{(1-b)}$$
$$D+T\rightarrow {}^4He(3.5MeV)+n(14.1MeV) \quad \text{(2)}$$
$$D+{}^3He\rightarrow {}^4He(3.6MeV)+p(14.7MeV) \quad \text{(3)}$$

In the fusion reactions shown in Eq. (1) there are two equally likely D-D fusion reactions. The (1-a) reaction produces a ^{3}He but (1-b) reaction produces a triton. The ^{3}He will fuse with the background deuterium. Permitting the tritium to fuse leads to the catalyzed DD fuel cycle. Therefore, because the D-T reaction would produce an energetic (14.1MeV) neutron and since that generated neutrons are hard to control, we propose to remove the triton before a substantial fraction can fuse and replace it with the ^{3}He tritium decay product. This leads to the generation of 22 MeV of energy per D-D fusion reaction. This fusion cycle is known as "Helium catalyzed D-D" fusion. Assuming that tritium produced by D-D reaction and ^{3}He product can be transferred to plasma, the rate of deuterium production is:

$dn_D/dt=S_D-0.5n_D^2<\sigma v>_{DD,n}-0.5n_D^2<\sigma v>_{DD,p}-n_Dn_T<\sigma v>_{DT}-n_D n_{3he}<\sigma v>_{D3He}-n_D/\tau_p$ (4)

$S_D=2.65\times10^{22}$ is the source rate of deuterium production and τ_p is the particle confinement time. Production rates of ^{3}He for two states such as without and with catalyzed processes are given by the following Eqs.

$dn_{He3}/dt= - n_{3He}/\tau_p+0.5n_D^2<\sigma v>_{DD,n}-n_{He3}n_D<\sigma v>_{DHe3}$ (5) (Without considering catalyzed process)

$dn_{He3}/dt= - n_{3He}/\tau_p+0.5n_D^2<\sigma v>_{DD,n}+n_T/\tau_p-n_{He3}n_D<\sigma v>_{DHe3}$ (6)   (With considering catalyzed process)

The tritium density is obtained from the D-T rate Eq:

$dn_T/dt=0.5n_D^2<\sigma v>_{DD,p}-n_Dn_T<\sigma v>_{DT}-n_T/\tau_p$ (7)

These Eq.s determine the fraction of non-deuterium ions which is low compared to the deuterium density. Finally, the proton, neutron and alpha (^{4}He) rate Eqs and the balance Eq. of energy production are written as follows, respectively:

$dn_p/dt=-n_p/\tau_p +n_D^2/2 <\sigma v>DD_{,P} +n_Dn_{3He} <\sigma v>_{DHe3}$ (8)

$dn_p/dt=-n_n/\tau_p +n_D^2/2 <\sigma v>DD_{,n} +n_D n_T <\sigma v>_{DT}$ (9)

$dn_{4He}/dt=-n_{4He}/\tau_p +n_{3He}n_D <\sigma v>_{DHe3}+n_Tn_D <\sigma v>_{DHe3}$ (10)

$dE/dt=-E/\tau_E +Q_{D3He}n_Dn_{3He} \langle\sigma\upsilon\rangle_{D3He}+Q_{DT}n_Dn_T\langle\sigma\upsilon\rangle_{DT}+0.5Q_{DD,p}n_D^2\langle\sigma\upsilon\rangle_{DD,p}+0.5Q_{DD,n}n_D^2\langle\sigma\upsilon\rangle_{DD,n}-P_{bremsDD}-P_{bremsDHe3}-P_{bremsDT}$ (11)

The required condition for neutralizing charge is: $n_D+n_T+2n_{He} =n_e$. In addition, Q_{D3He}. Q_{DT}. Q_{DD}. $P_{bremsDHe3}$. $P_{bremsDT}$ and $P_{bremsDD}$ represent the energy and bremsstrahlung energy generated by D-D fusion reactions, and side reactions of D-T,D-^{3}He, respectively. So that:

$P_{brems}=4.85\times10^{-37}\times z_{eff} n_e^2 \sqrt{T}$ (W.m^3/keV)   (12)

And the reactivity of these fusion reactions is determined by the sigma-v parameter, which is defined as the product of average cross-section into the relative velocity of the two fusion nuclei. This averaging is performed on the relative velocity distribution functions of the two nuclei. Therefore, the sigma-v parameter is generally defined as:

$<\sigma v>=C_1\theta e^{-3\mu} \sqrt{\mu/m_r c^2 T^3}$ (13)

Where μ θ and B_G follow the following relationships:

$$\begin{cases} \mu = (\frac{B_G^2}{4\theta})^{\frac{1}{3}} \\ \theta = \frac{T}{\left[1-\frac{T(C_2+T(C_4+TC_6))}{1+T(C_3+T(C_5+TC_7))}\right]} \\ B_G = \pi\alpha Z_1Z_2\sqrt{2m_rc^2} \end{cases}$$ (14)

It should be noted that the constant values of C_1 to C_7 are given in Table 1. Fig. 1 shows the temperature variations of $<\sigma v>$ for the described fusion reactions.

As can be seen, the D-T reaction is most likely to occur but the branch DD-p reaction has a minimum. By solving the point kinetic nonlinear differential Eqs 4 to 11, we obtain the time dependent density, net energy and following that energy gain of each fusion reaction and finally produced proton flux, for two cases of with / without catalyzed ^{3}He (see Figs 2 to 4).As can be seen in Fig. 2A, the density of deuterium fusion nuclei decreases with time, because with increasing time the reactants have decreased. But our calculations show that temperature variations do not have much effect on the density of the fusion deuterium nuclei. From observing figures 2 to 4, we find that except for plots A, B and C in Figure 2, the rest of the graphs behave similarly with increasing time and temperature, so that with increasing temperature, the desired quantities increase.

Also, by studying the temporal behavior of these quantities at each temperature, we find that for two cases (with and without Helium catalyzed DD) with increasing time, each of the mentioned quantities first increases and then decreases and finally reaches its stable value. Also, for helium-3 in the case of helium-catalyzed, with the enhancement of the temperature and time at first

Table 1. Constant values C_1 to C_7 in eq. 14

	T(d.n)⁴He	D(d.n)³He	D(d.p)T	³He(d.p)⁴He
C_1	1.17E-09	5.43E-12	5.66E-12	5.51E-10
C_2	1.51E-02	5.86E-03	3.41E-03	6.42E-03
C_3	7.52E-02	7.68E-03	1.99E-03	-2.03E-03
C_4	4.61E-03	0.00E+00	0.00E+00	-1.91E-05
C_5	1.35E-02	-2.96E-06	1.05E-05	1.36E-04
C_6	-1.07E-04	0.00E+00	0.00E+00	0.00E+00
C_7	1.37E-05	0.00E+00	0.00E+00	0.00E+00
(keV) $m_r c^2$	1124656	937814	937814	1124572
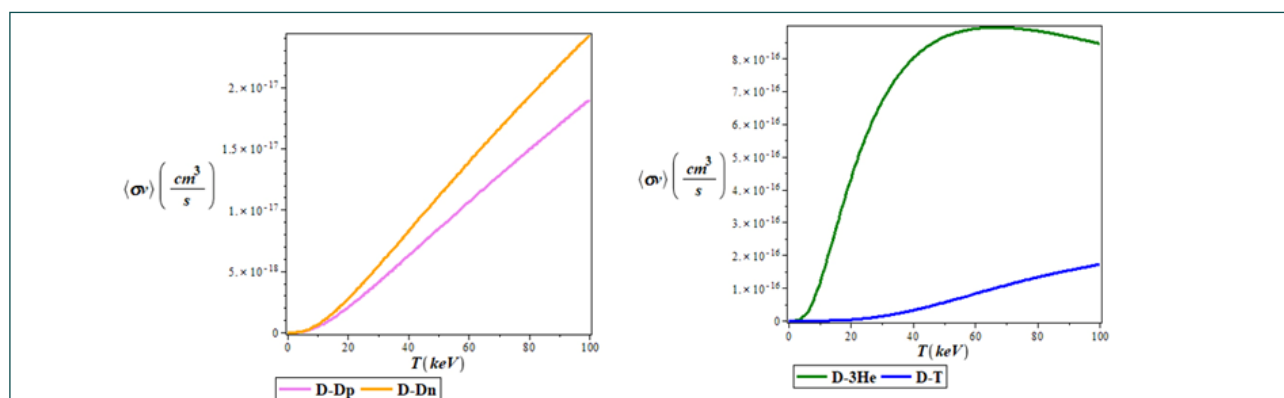
Figure.1. Temperature variations of $\langle \sigma v \rangle$ for different fusion reactions

it is increased gradually with time and then reaches to the steady state. The gain of fusion energy is: $G=E_{out}/E_{in}$ where E_{out} is the fusion energy released and E_{in} is the incident laser energy on the fuel. Our calculations give a maximum gain of approximately 25 at T = 100keV and t=2.029×10⁻¹⁰s with E_{in}=0.1 M J taking into account the helium catalyzed, whereas without the helium catalyzed G is 6.5 at the same conditions. (See Figure 4).

3-Cross section and production rate of Fluorine-18

The rate of radionuclide production depends on a number of factors, including the magnitude of the cross-section reaction in terms of the energy function, the energy of colliding particles, and target thickness in terms of the number of nuclei per cm², which determine the energy of the output particles. The production rate of ¹⁸F¹⁸F is determined by the following relation:

$$-\frac{dn}{dt} = R = nI(1 - e^{-\lambda t}) \int_{E_0}^{E} \frac{\sigma(E)}{dE/dx} dE \qquad (15)$$

Where R is the number of nuclei produced per second; n is the target thickness in units of nuclei per cm²; I is the particle flux per second and corresponds to the beam flow; λ is the decay constant and is equal to $(\ln 2)/T_{1/2}$; t is the time of irradiation in seconds; σ is the cross-section of reaction, or probability of interaction, whose unit is cm2 and is a function of energy (see Fig. 5); E is the energy of the incident particles; x is the traveled distance by particle; dE/dx is the stopping power and $\int_{E_0}^{E}$ is the integral that contains the initial energy to the final energy of the incident particles along the path.

4-Saturation coefficient
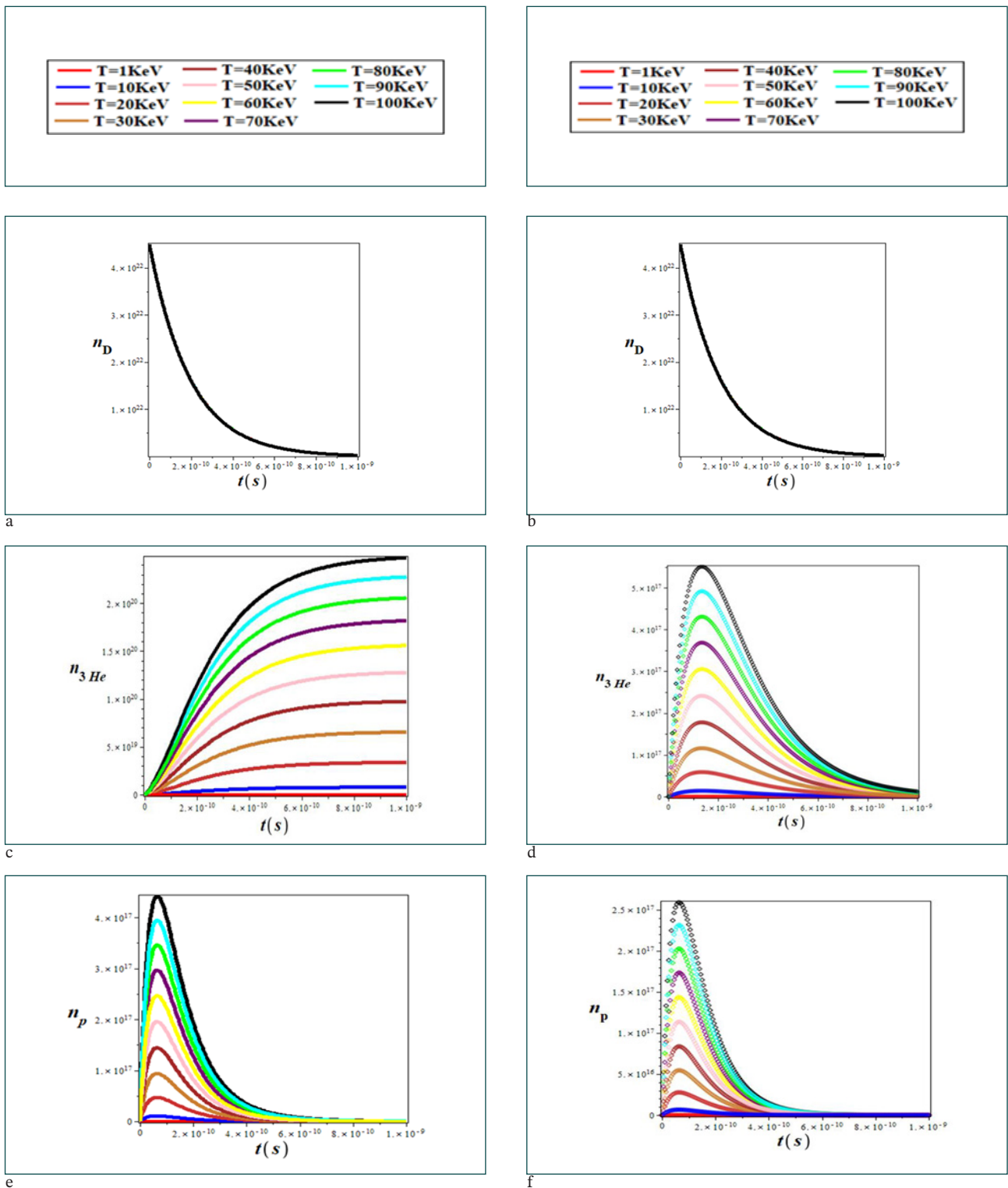
At shorter irradiation time, the product fraction is relat-

Figure.2. time variations of particle densities (cm^{-3}) A,B: Deuterium ,C,D: Helium-3 and E,F :Proton at the temperature range of 0≤T(keV)≤100.(Hint: solid line and point line are related to with and without ^{3}He catalyzed ,respectively)
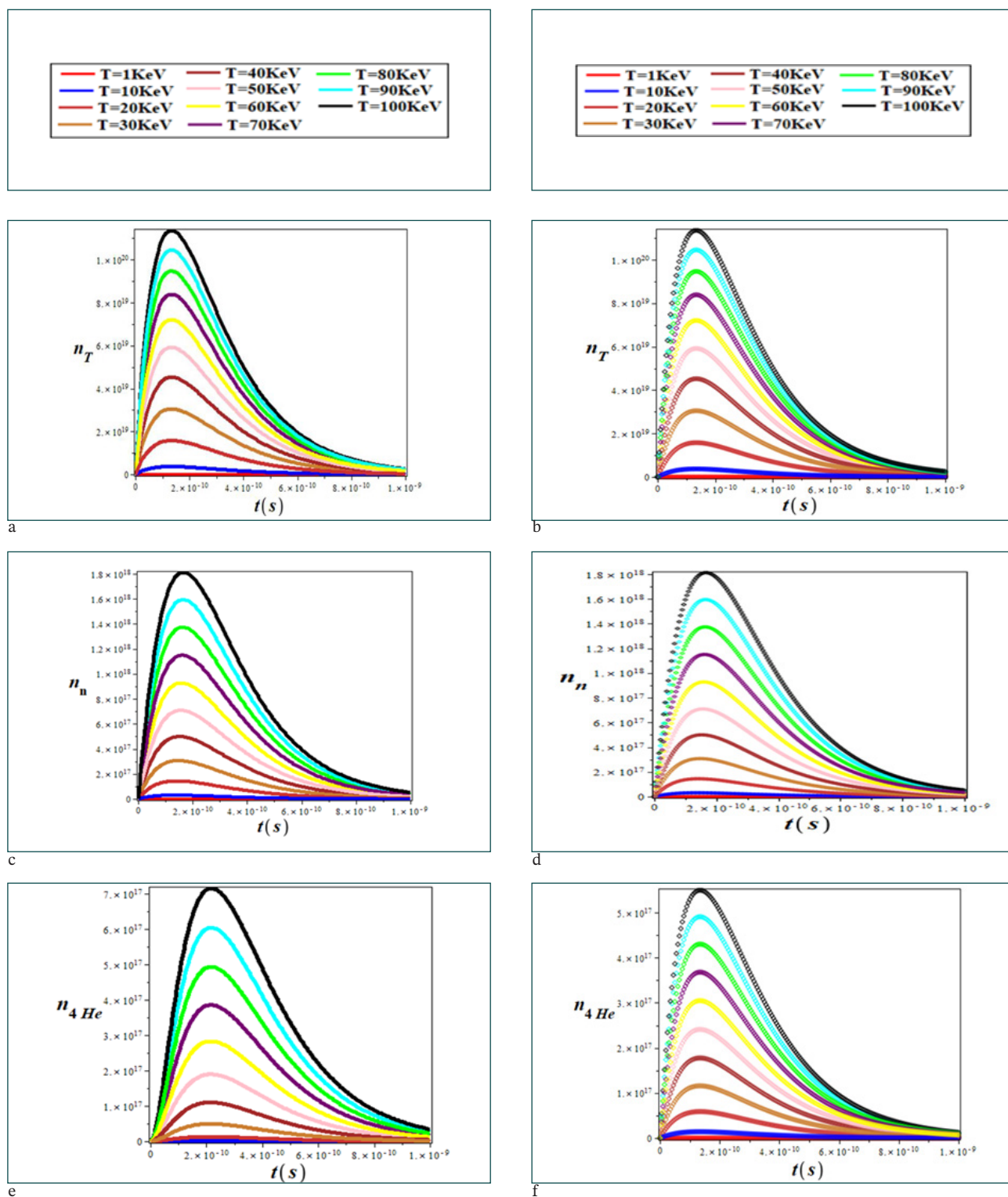
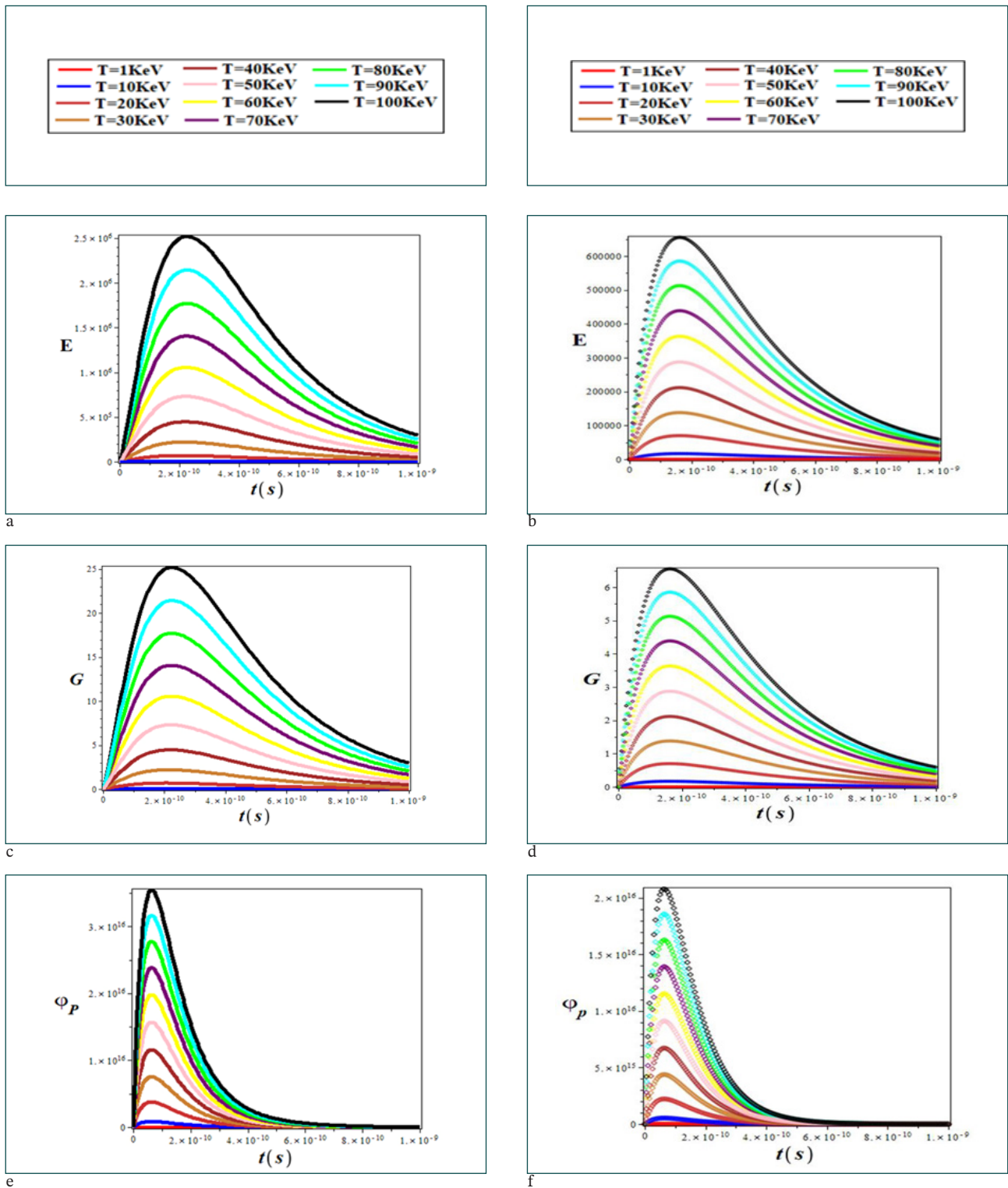**Figure.3.** time variations of particle densities(cm⁻³) A,B: Tritium ,C,D: Neutron and E,F :Hellium-4 at the temperature range of 0≤T(keV)≤100. (Hint: solid line and point line are related to with and without ^{3}He catalyzed ,respectively)

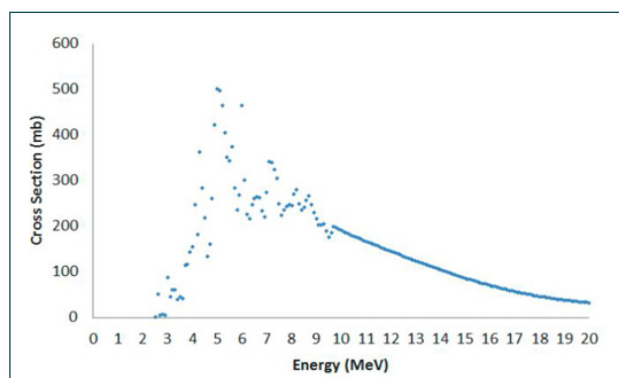**Figure.4.**time variations of A,B: Fusion energy(J) ,C,D: Energy gain and E,F :Generated proton flux (cm^{-2}) s^{-1}) at the temperature range of 0≤T(keV)≤100. (Hint: solid line and point line are related to with and without ^{3}He catalyzed ,respectively)

Figure.5. the variations of production of ^{18}F corresponding to the reaction ^{18}O(p.n)^{18}F versus energy
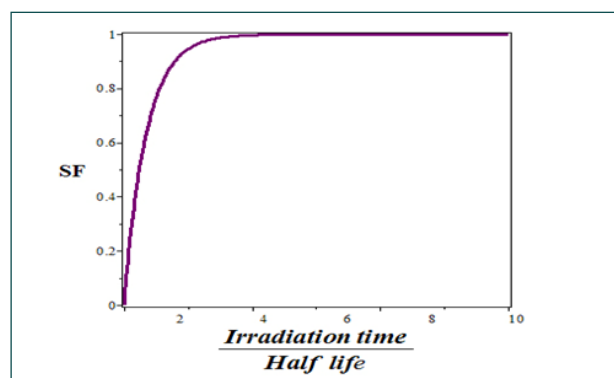

Figure.6. variations of saturation coefficient as a function of the ratio of the irradiation time to half-life of the radionuclide produced by the ^{18}O(p, n)^{18}F reaction

ed to the saturation factor (SF), denoted by 1-e$^{-\lambda t}$, where λ is the nuclear decay constant and t is the time of the bombardment. Clearly, irradiation with a half-life is equivalent to one half-life in which leads to a 50% saturation. For practical reasons, irradiation rarely exceeds three half-lives (90% saturation). The practical production limits of a given radionuclide are determined by the isotope half-life. It is relatively easy to reach saturation to produce ^{15}O with a half-life of 2 minutes. But it is not reasonable for a irradiated target to produce 18F to the saturation point because it requires too long irradiation times. In Fig. 6, we plotted the variations of saturation coefficient in terms of the ratio of the irradiation time to half-life of the radionuclide produced by the ^{18}O (p, n)18F reaction.

5-Production yield of Fluorine-18

Since that the kinetic energy of the particle is slowly reduced by passing through a layer of thick target atoms, the production yield of $(_{}^{18})$F on the thick target is given by the following relation:

$$\text{Yield} = \frac{3.76.10^9}{Z.M} \int_{E_{\text{thershold}}}^{E_{\text{max}}} \frac{\sigma(E)}{\frac{dE}{dx}} dE(1 - e^{-\lambda t}) \, {MBq}/{\mu A} \qquad (16)$$

Where Z is the atomic number of incident particle, M is the mass number of the target atoms $E_{\text{thershold}}$ to E_{max} ,is the energy interval, σ (E) is the cross section at energy E, dE / dx is the total stopping power at the target, which is discussed below. λ is the decay constant and t is the

irradiation time (0 to 80 h). The unit of yield production is MBq/μA (due to the coefficient of 3.76.10^9).In Figure 7, we show the time variations of the yield production of ^{18}Fin water. It is seen that the yield production of ^{18}F gradually increases and reaches steady state after 15 hours.

6-Stopping power, radiation yield, CSDA range and Fluorine-18 absorbed dose in water

SStopping power, CSDA range, absorbed dose of ^{18}F in water are divided into two groups using Monte Carlo Gate7 / Geant-4 simulation code: Group 1: Heavy charged particles such as alpha and proton, Group II: Light charged particles such as electrons and positrons. Each group has specific interactions with biomaterials that related to the mass difference between them. Isotope ^{18}F is a beta emitter with a half-life of 109.77 minutes which is used in medical imaging. This isotope is one of the anticancer drugs used in the diagnosis, regulation and "treatment de-
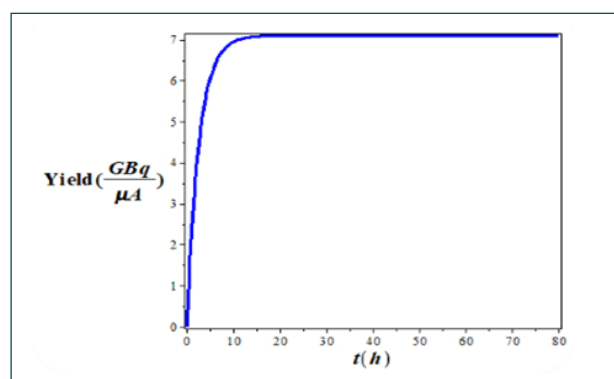

Figure.7. yield production of ^{18}Fin water versus time

cision" of many cancers related issues. Beta particles lose its energy in interaction with matter through two mechanisms. The first mechanism, so-called "collision loss", that results in excitation (electrons move to higher energy levels) and ionization (unbound state) of matter where large scattering angles more deflected heavy charged particles from their direct path. The second mechanism is the "radiative loss" that results in the emission of electromagnetic radiation (bremsstrahlung radiation) resulting from the acceleration of the particle. It usually does not matter for heavy charged particles because the magnitude of the bremsstrahlung radiation is proportional to the reciprocal square of the mass. The amount of energy transferred from the ionizing particle to biological targets is important for tumor radiotherapy and should be accurately estimated. The stopping power depends on the type of radiation, the amount of energy, and the environmental characteristics that the particle passes through Different studies have been done on the design of computational models to estimate this physical quantity. The stopping power formula involves the Coulomb interaction of heavy charged particles in the material. Also there is another formula that calculates energy losses through bremsstrahlung radiation [15,16]. Development is continuing in this field and the appropriate formula for the particle stopping power due to the Coulomb interaction has been defined by Tsoulfanidis et al. [17]. In this work, the collision stopping power properties of positrons in water in the energy range of 10 eV to 10 keV are investigated using two formulas that incorporate the benefits of data obtained in PET imaging [17-19]. In another study, the modified stopping power formula for low and medium energy positrons for different targets (water, Al, Cu and Si) is presented [20]. The collision power or mechanism of radiation energy loss depends on the energy of the particles. In low-energy beta collisions, energy loss is predominant in radiation, while in high energy, radiation energy loss is the predominant mechanism that results in more bremsstrahlung radiation [18]. The risk of beta-particle bremsstrahlung radiation can be explained by the Y-radiation yield, which is defined as the average energy fraction that a beta particle radiates. The stopping power and the Continues Slow-

ing Down Approximation Range, R_{CSDA}, (the path length of the irradiated particle in the target), which is related to the amount of absorbed dose D (energy loss per unit mass), can be calculated. The electron paths in matter are similar to the positron paths in matter, and the stopping power and range are almost the same for the equal initial energy. Monte Carlo simulation has a high degree of performance that is capable of covering all theoretical calculations of stopping power and cross section. This improves limited problems in the field, such as the angles of scattering of radiation particles, the ionization and excitation process, and the change of energy dissipation of particles in the environment. The purpose of this work is calculation and estimation of the stopping power, R_{CSDA}, absorbed dose in water using Monte Carlo simulation. To understand this, the kinetic energy of the particles at the end of each annihilation process must be taken into account in the energy loss calculations for a particle. In this work, we simulate a positron ^{18}F point source in the water at the center of a homogeneous environment (0,0,0) with a sufficient number of events. At the end of each annihilation process, the paths are presented with Cartesian coordinates (x, y, z) and energy loss values. In.the following the Bethe-Bloch relativistic Eq. for calculating the stopping power of a light particle is given, which contains the sum of the two components of the collision and radiative stopping power [21,22]:

$$-\left(\frac{dE}{dx}\right)_{tot}^{\mp} = \left(-\left(\frac{dE}{dx}\right)_{coll}^{\mp}\right) + \left(-\left(\frac{dE}{dx}\right)_{rad}^{\mp}\right) \qquad (17)$$

The expression of the collision stopping power $-\left(\frac{dE}{dx}\right)_{coll}^{\mp}$ is as follows:

$$-\left(\frac{dE}{dx}\right)_{coll}^{\mp} = \frac{4\pi k^2 e^2}{mc^2\beta^2}\left[\ln\frac{mc^2\tau\sqrt{\tau+2}}{I\sqrt{2}}F^{\mp}(\beta)\right] \qquad (18)$$

$$F^{-}(\beta) = \frac{1-\beta^2}{2} + \frac{1-\beta^2}{2(\tau+1)^2}\left[\frac{\tau^2}{8} - (2\tau+1)\ln 2\right] \qquad (19)$$

$$F+(\beta)=\ln 2 - \beta^2/24\left[23 + 14/\tau+2 + 14/(\tau+2)^2 + 14/(\tau+2)^3\right] \qquad (20)$$
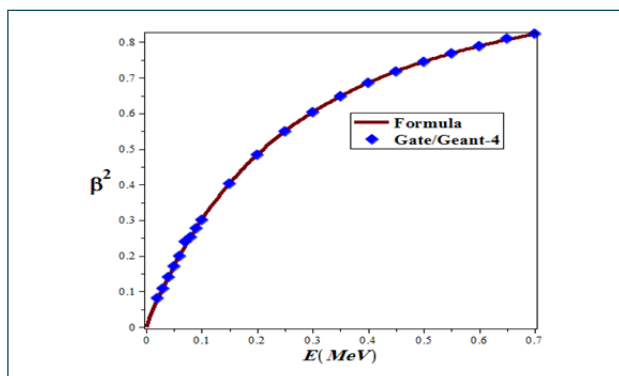
Figure.8. Comparison of β^2 variations in terms of particle energy in water at the range of $0.02 \leq E(MeV) \leq 0.7$ using the Monte Carlo Gate / Geant-4 simulation code and the formula $\beta^2 = 1-(1+E/(mc^2))^{-2}$

Figure.9. variations of the ratio of kinetic energy to resting positron energy ($\tau = E/(mc^2)$) in the energy range of $0.02 \leq E(MeV) \leq 0.7$ in water

Remember that negative and positive signs refer to electrons and positrons, respectively. For β^+, $\tau = E/mc^2$ is the kinetic energy of the beta particle, expressed in terms of the mass of the electron, and $\beta^2 = v^2/c^2 = 1-(1+E/mc^2)^{-2}$ where v is the particle velocity, c is the velocity of light in the vacuum, and k = Coulomb constant. In Fig. 8 ,the variations of β^2 in terms of particle energy in water in the range of $0.02 \leq E(MeV) \leq 0.7$ are compared to Monte Carlo Gate / Geant-4 simulation code .As can be seen from Fig. 8, with increasing particle energy, β^2 is increased and the obtained results from Monte Carlo Gate / Geant-4 simulation code and formula $\beta^2 = 1-(1+E/mc^2)^{-2}$ are in good agreement.

Figure 9, shows the positron kinetic energy variations in the energy range of $0.02 \leq E(MeV) \leq 0.7$ in water. As can be seen from Fig. 9, as E increases, the positron kinetic energy grows linearly.

The average excitation energy for a material is obtained using the following empirical formula:

$$I_i = 19.0 \; eV \, , Z = 1 \qquad (21)$$

$$I_i \cong 11.2 + 11.7Z \;\; eV. \;\; 2 \leq Z \leq 13 \qquad (22)$$

$$nlnI = \sum_i N_i Z_i lnI_i \qquad (23)$$

Where: I = the average excitation energy in the environment in eV, n is the electron density of the matter, and Z is the atomic number. When we put these components in Eq. 18, the formula for the stopping power
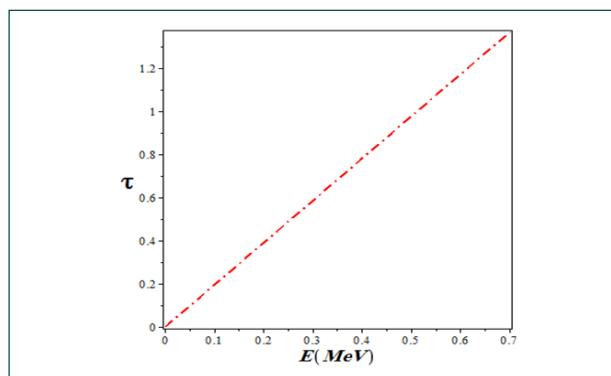
effect is as follows:

$$-\left(\frac{dE}{dx}\right)^{\mp}_{coll} = \frac{5.08 \times 10^{-31} n}{\beta^2} \left[\ln \frac{3.61 \times 10^5 \tau \sqrt{\tau + 2}}{I(eV)} + F^{\mp}(\beta) \right] \qquad (24)$$

and the radiative stopping power $-(dE/dx)^{\mp}_{rad}$ is given by the following relation:

$$-\left(\frac{dE}{dx}\right)^{\mp}_{rad} = \left(\frac{dE}{dx}\right)^{\mp}_{coll} \times \left(\frac{dE}{800}\right) \qquad (25)$$
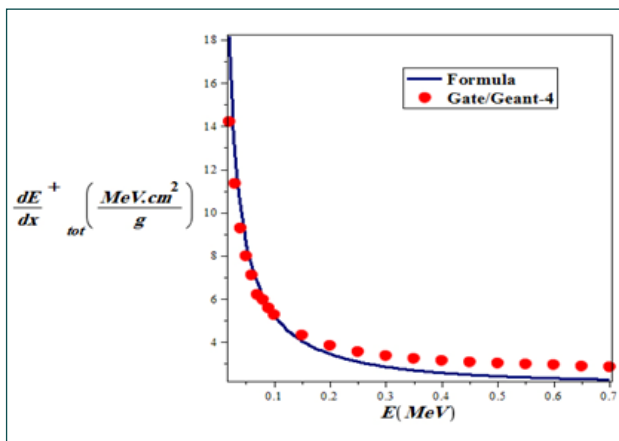
In Fig. 10, we compare the variations of the collisional, radiative and total positron mass stopping power in terms of particle energy in water in the range of $0.02 \leq E(MeV) \leq 0.7$ using the Monte Carlo Gate / Geant-4 simulation code and the formulas were utilized in Eqs.17, 24 and 25. As can be seen from Fig. 10, the positron collision mass stopping power is decreased by increasing E, and its radiative stopping power is increased, and since that positron collision mass stopping power is dominated by its radiative stopping power, such that it decreases the total positron mass stopping power by increasing E. The results of the Monte Carlo Gate / Geant-4 simulation code and formulas 17, 24 and 25 are in good agreement. Also, to make a comparison of the mass stopping power of the collision, radiative, and the total positron and electron through the Bethe-Bloch theory, we plotted Figs. 11A, B and C. From these figures, it can be seen that at low energies these powers are very close for the positron and the electron, but with increasing energy they diverge and the positron mass stopping power less than
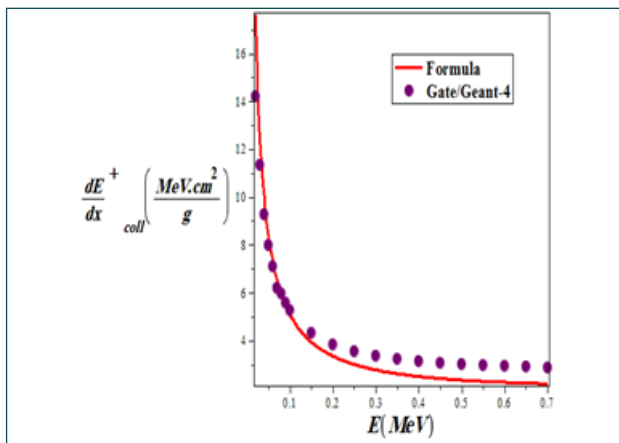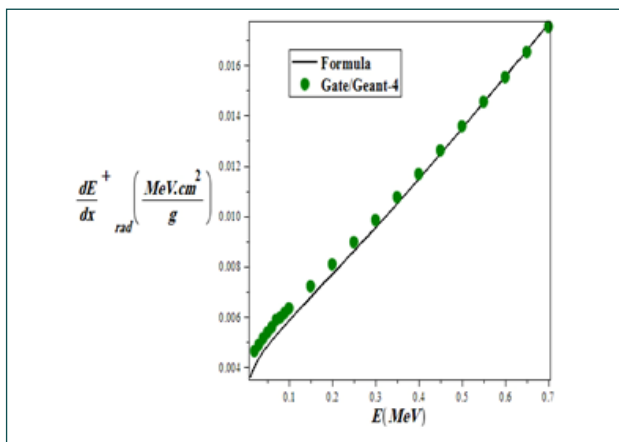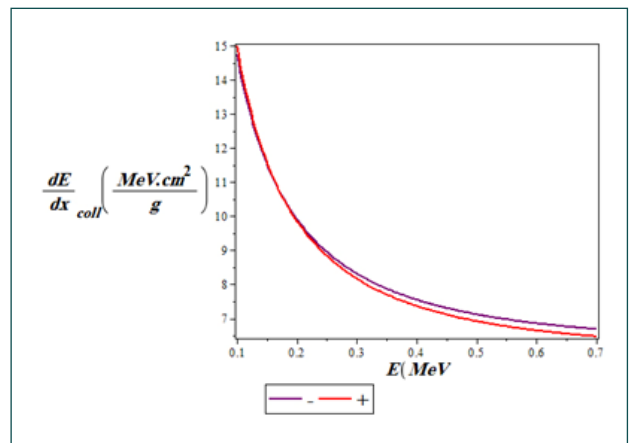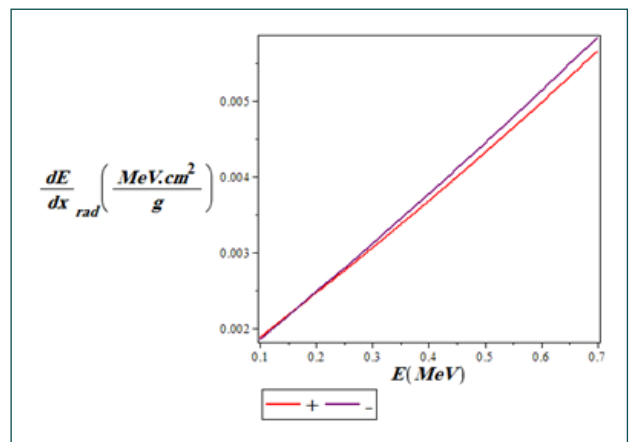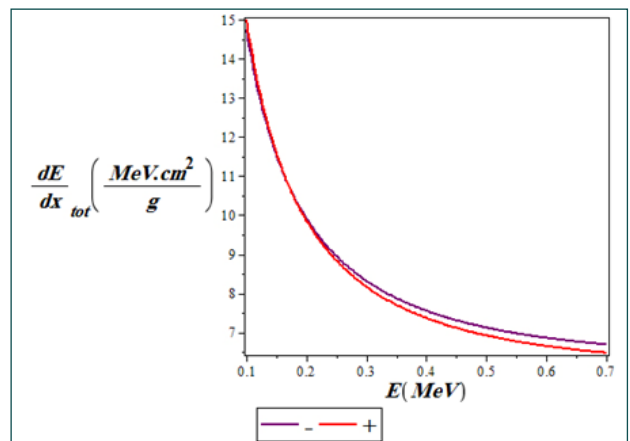
a

b

c

Figure.10. Comparison of mass-stopping power variations A: Collision B: Radiative C: Total positron versus particle energy in water in the range of 00.02≤E(MeV)≤0.7 using the Monte Carlo Gate / Geant-4 simulation code and the formulas presented in Eqs. 17, 24 and 25

a

b

c

Figure.11. Comparison of mass-stopping power variations A: Collision B: Radiative C: Total positron and electron in terms of particle energy in water in the range of 0.02≤E(MeV)≤0.7 using the formulas presented in Eq.s 17 (Bethe-Bloch theory), 24 and 25
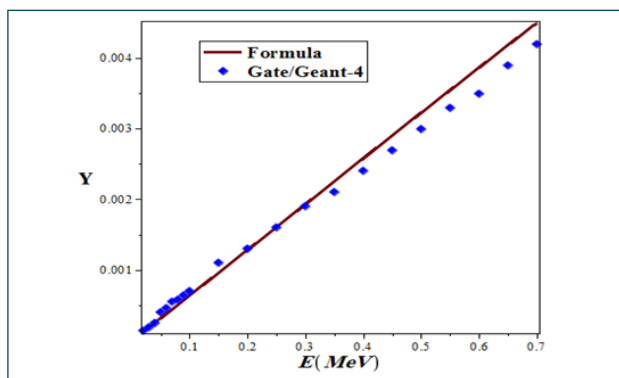
Figure.12. Comparison of beta particle radiation yield variations in terms of particle energy in water in the range 0.02≤E(MeV)≤0.7 using Eq. 26 and Monte Carlo Gate / Geante-4 simulation code
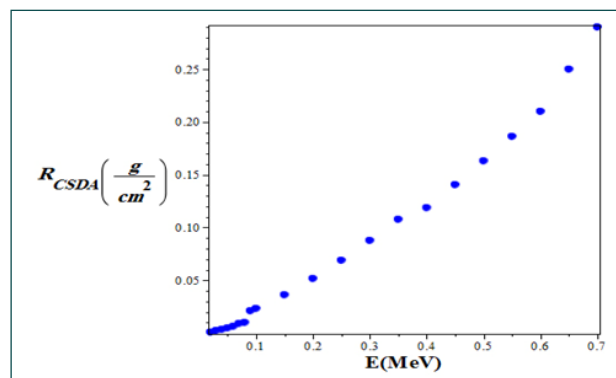

Figure.13. R_{CSDA} variations using Geant4/Gate7 simulation code in terms of kinetic energy of positive beta particle using Eq. 27
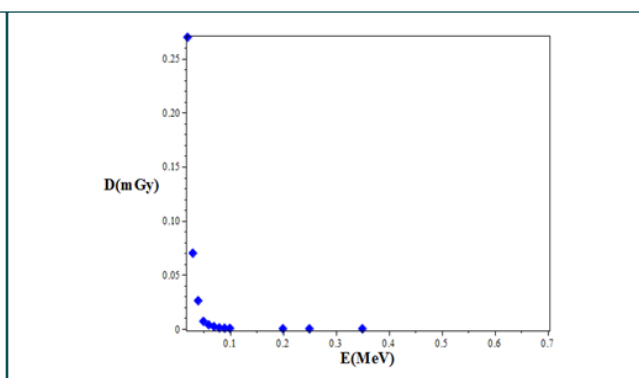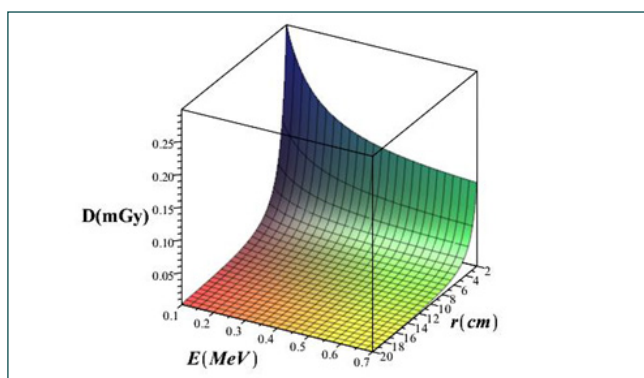

Figure.14. variations of A: 3D absorbed dose using Equ.28 B: Two dimensional absorbed dose using Gate / Geant-4 simulation code in terms of particle energy and distance in water

the electron mass stopping power.

For a beta particle of energy E in MeV passing through a material with atomic number Z the radiation yield (Y) is expressed as follows [23]:

$$Y \cong 6 \times 10^{-4} ZE / 1 + 6 \times 10^{-4} ZE \quad (26)$$

In Fig. 12, we present the variations of the beta particle's radiation yield in terms of particle energy using Eq. 26 and Monte Carlo Gate / Geante-4 simulation code. As can be seen from this figure, they are in good agreement at low energies and gradually distant at higher energies. The mass stopping power $-(dE/\rho dx)^{\mp}_{total}$ (MeV.cm²/g) is obtained from the ratio of Eq. 17 to the target density. By integrating on the inverse of $-(dE/\rho dx)^{\mp}_{total}$ from E (MeV) to zero the value of R_{CSDA} (g/cm²) is given by:

$$R_{CSDA} = \int_E^0 dE / -(dE/\rho dx)^{\mp}_{total}) \quad (27)$$

In Fig. 13, we see that the R_{CSDA} variations using the Geant4/Gate7 simulation code in terms of the kinetic energy of a positive beta particle. As can be seen by increasing the beta particle energy the value of R_{CSDA} increases.

The absorbed dose D(MeV/g)is obtained by dividing R_{CSDA} to the target density to obtain the distance r (cm) that the particle travels in the medium [24]:

$$D = -(dE/\rho dx)^{\mp}_{total} / 4\pi \rho r^2 \quad (28)$$

Using Eq. 28, we calculate the absorbed dose in water and plot its three-dimensional diagram in terms of particle energy and distance variations in Fig. 14. As can be seen from the graph, the absorbed dose values of the computational method and are consistent with simulating method.

7-Steps in the synthesis and purification of FDG

The typical steps taken during FDG synthesis are summarized in the following:

Step 1: Irradiation of [18]O water with protons.

Step 2: Extraction of [^{18}F] fluoride from the H_2[18]O target.

Step 3: Drying of [^{18}F] fluoride.

Step 4: Labelling of the mannose triflate with the [18]F.

Step 5: Removal of the protective acetyl groups by hydrolysis to form FDG.

Step 6: Purification and formulation of the final FDG product

Step 7: Sterilizing filtration.

Step 8: Sampling for quality control and quality assessment.

Step 9: Dispensing.

Step 10: Packaging and shipping.

Since protons are used in the first step for irradiating of [18]O water, therefore we explain only this step and the details of the other steps are found in Ref. [25].

8-Irradiation of [18]O water with protons

The [18]O(p,n)[18]F reaction with 18O enriched water produces [18]F. Typical irradiation parameters include:(I) [18]O enrichment, typically >95%; (II) Chemical purity of [18]O enriched water, higher than 99.99%;(III) Target volume, ranging from 0.5 to 2.5 mL;(IV) Proton beam of 8–19 MeV;(V) Beam currents of 20–100 μA; (VI) Irradiation time from 30 min to 3 h. A detailed discussion of cyclotron targetry and radionuclide production is beyond the scope of this article, but can be found in the literature, including Refs [26, 27].

The total amount of [^{18}F] fluoride which can be generated is dependent on energy, beam current and irradiation time. Other factors influencing total yield will be [18]O enrichment in water, chemical purity of enriched water, target material, target volume and target design. One can expect approximately 111 GBq (3 Ci) of [^{18}F] fluoride in a single target during one hour of irradiation with a 10–13 MeV proton beam at a beam current of 50 μA, and approximately 167 GBq (4.5 Ci) for a higher energy machine (14–19 MeV). The yield can be enhanced by increasing beam current and irradiation time as well

as by using dual targets. The chemical purity of enriched water is critical for longer irradiations with high beam currents. The benefit of longer irradiation needs to be carefully optimized, as the yield reaches a saturation point with long irradiations. Also, heat generated within a target limits the beam current that may be put onto a target. Nevertheless, with a customary useful FDG yield of >65%, several curies of FDG can be produced in a single irradiation/production cycle for in-house use, as well as for distribution to other PET centers. The oxygen-16 present in the target water leads to the production of 13N through an (n,α) reaction, which is a radionuclidic impurity. Nitrogen-13 is a radionuclide decaying through positron emission with a half-life of 10 minutes and hence a major part of the ^{13}N will decay during the synthesis of FDG, leaving trace amounts. Nitrogen-13 can appear in several chemical forms including nitrate, nitrite, nitrogen and ammonia, depending on target conditions. Also, depending on the method of synthesis and purification of FDG, some amount of ^{13}N may be present in final product which will be result in a shorter measured half-life.

Since at this stage it is necessary to use protons in the energy range of 8-19 MeV and beam currents of 20–100 μA, this spark entered our minds that the occurrence of D-D fusion reactions and side reactions can be used as a source to generate electrical energy and also to produce [18]FDG radioisotope for PET imaging. It should be noted that the cost of Positron Emission Tomography (PET) with [([18]) F]-fludeoxyglucose (([18]) F-FDG) studies is mainly influenced by the price of the radiopharmaceutical, which may vary throughout Europe from 300 to 500 Euro per patient dose (370 MBq). Since that for producing of this radioisotope requires a cyclotron accelerator to accelerate the protons which is expensive ,therefore if the produced protons from the DD and D-[3]He fusion reactions are used with the energy of 3.02MeV and 14.7MeV,respectively we will need smaller and less expensive cyclotron accelerators and as a result will reduce the cost of final production of this radioisotope.

9-Conclusion

Since that PET imaging requires radioisotopes with a half-life of less than two hours, PET scans are often installed in the vicinity of an accelerator. The most widely used of these isotopes is ^{18}F, which has a half-life of about 110 minutes. The cost of building and installing such accelerators is about one million dollars. Therefore, this paper presents a theoretical review of a novel method for the production of ^{18}F by employing proton production through the main fusion reaction D(d;p)T and side fusion ^{3}He(d;p) ^{4}He with and without helium catalyzed. It should be noted that the energy released from these fusion reactions are clean energy and it can be convert to electric energy. This study is also dedicated to developing a numerical analysis of stopping power, absorbed dose, and cross sections related to positrons collisions with water. Such quantitative studies are very useful for predicting the health status of patients at risk and for scientifically understanding the annihilation of photons in the environment. These results are definitely used to optimize patient exposure and effectively radiation the whole body without significantly reducing image quality.

REFERENCES

1. Basu S. Fundamentals of PET and PET/CT imaging. Ann. N. Y. Acad. Sci. 2011; 1228: 1–18.
2. Fischer BM. PET/CT is a cost-effective tool against cancer: synergy supersedes singularity. Eur J Nucl Med Mol Imaging. 2016;43: 1749–1752.
3. Marcu LG, Moghaddasi L and Bezak E. Imaging of Tumor Characteristics and Molecular Pathways with PET: Developments Over the Last Decade Toward Personalized Cancer Therapy. Int J Radiat Oncol .2018; 102: 1165–1182.
4. Cherry SR. Total-body imaging: transforming the role of positron emission tomography. Sci Trans Med. 2017; 9: 381-389.
5. Oelfke U. Proton dose monitoring with PET: quantitative studies in Lucite Phys Med Biol. 1996; 41: 177-186.
6. Parodi K, Enghardt W and Haberer T. In-beam PET measurements of β+ radioactivity induced by proton beams. Phys Med Biol. 2002; 47 :21-26.
7. Paans AMJ and Schippers JM. Proton Therapy in combination with PET as monitor: A feasibility study. IEEE Trans Nucl Sci. 1993; 40 :1041-1043.
8. Litzenberg D. On-line Monitoring and PET Imaging of the Positron-Emitting Activity Created in Tissue by Proton Radiotherapy Beams. Ph.D. Thesis, Univ. of Michigan. 1997.
9. Nakai S and Mima K, Reports on Progress in Physics. 2004; 67: 321–349.
10. Atzeni S and Meyer-Ter-Vehn J. The Physics of Inertial Fusion, Oxford Science Publications. 2004.
11. Cañadas M, Arce P, and Rato Mendes P. Validation of a small-animal pet simulation using gamos: A GEANT4-based framework. Phys Med Biol. 2011;56: 273– 288.
12. Assie K, Gardin I, Vera P and Buvat I . Validation of the Monte Carlo simulator GATE for Indium 111 imaging. Phys Med Biol. 2005; 50:3113–3125
13. Bethe H. Bremsformel für Elektronen relativistischer Geschwindigkeit. Zeitschrift für Physik. 1932; 76: 293–299.
14. Ziegler, J. F. Stopping of energetic light ions in elemental matter. Journal of Applied Physics 1999; 85: 1249–1272.
15. Bloch F. Zur Bremsung rasch bewegter Teilchen beim Durchgang durch Materie. Annalen der Physik. 1933; 408:285–320.
16. Rohrlich F, Carlson BC. Positron–electron differences in energy loss and multiple scattering. Physical Review. 1954; 93:38–44.
17. Tsoulfanidis N. Measurement and detection of radiation. 2nd Edition. Taylor & Francis, Washington; 1995: 1–636.
18. Tanır G, Bölükdemir MH, Keleş S, Göker I. On the stopping power for low energy positrons. Chinese Journal of Physics. 2011; 50:1–9.
19. Gümüş H. New stopping power formula for intermediate energy electrons. Applied Radiation Isotopes. 2008; 66:1886–1890.
20. Gümüş H, Kabaday O, Tufan CM. Calculation of the

stopping power for intermediate energy positrons. Chinese Journal of Physics. 2006; 44:290–296.

21. Krane K. Modern Physics. 2nd Edition. Department of Physics, Oregon University. John Wiley & sons Inc USA; 1996: 145.

22. Atoms JET. Radiation and Radiation Protection. 3rd Edition. Completely Revised and Enlarged Edition. WILEY-VCH Verlag GmbH & Co. KGaA, Weinheim Germany; 2007: 606.

23. Koch HW, Motz JW. Bremsstrahlung cross section formulas and related data. Reviews of Modern Physics. 1959; 31:920–55.

24. Prestwich WV, Nunes J, Kwok CS. Beta dose point kernels for radionuclides of potential use in radioimmunotherapy. Journal of Nuclear Medicine. 1989; 30:1036–46.

25. INTERNATIONAL ATOMIC ENERGY AGENCY, Cyclotron Produced Radionuclides: Guidance on Facility Design and Production of [18F]Fluorodeoxyglucose (FDG), 2012, VIENNA.

26. INTERNATIONAL ATOMIC ENERGY AGENCY, Cyclotron Produced Radionuclides: Principles and Practice, Technical Reports Series , 2009,No. 465, IAEA, Vienna

27. INTERNATIONAL ATOMIC ENERGY AGENCY, Cyclotron Produced Radionuclides: Physical Characteristics and Production Methods, Technical Reports Series , 2009, No. 468, IAEA, Vienna.